Author's Post-print version. Article published in Energy & Fuels (ACS Publications):
DOI: 10.1021/ef5010557
Published version: https://pubs.acs.org/doi/abs/10.1021/ef5010557

Eulerian-Lagrangian Simulation of Biomass Gasification Behavior in a High-temperature Entrained Flow Reactor

Xiaoke Ku,* Tian Li and Terese Løvås

Department of Energy and Process Engineering

Norwegian University of Science and Technology (NTNU)

7491 Trondheim, Norway

ABSTRACT: In this paper, a multi-scale Eulerian-Lagrangian CFD model based on OpenFOAM has been constructed, which takes into account heat and mass transfer, pyrolysis, homogeneous and heterogeneous reactions, radiation, as well as the interactions between the continuous gas phase and discrete particles. The proposed model is validated and applied to a lab-scale biomass entrained flow reactor. The operating temperatures are high (1000-1400 °C) and influences of five operating parameters (reactor temperature, steam/carbon molar ratio, excess air ratio, biomass type, and particle size) on the gasification behavior are explored. Results show that an increase in the reactor temperature has positive effect on both the H_2 and CO productions; increasing the steam/carbon ratio increases the H_2 production but decreases the CO production; increasing the excess air ratio decreases both the H_2 and CO productions; the variations in the gas product for the four biomasses studied are not so significant due to similar biomass nature and hence one type can be replaced by another without any major consequences in the gasification performance; and both the CO and H_2 productions and carbon conversion decrease with an increase in particle size. Moreover, the predicted results follow the same trend as the experimental data available in the literature. Quantitative comparisons are also made and the agreement is good.

Author's Post-print version. Article published in Energy & Fuels (ACS Publications):
DOI: 10.1021/ef5010557
Published version: https://pubs.acs.org/doi/abs/10.1021/ef5010557

1. INTRODUCTION

Biomass is the world's fourth largest energy resource after coal, oil and natural gas. There are several methods of utilizing biomass to generate energy among which gasification appears to be more attractive due to its non-oxidation conditions and low pollutant emissions. Biomass gasification is a complex thermo-chemical process in which biomass is converted into synthetic gas (syngas) under sub-stoichiometric conditions. The syngas could be then used as a fuel in internal combustion engines, gas turbines, or fuel cells for the production of heat, mechanical energy, or power, or as a feedstock for the synthesis of liquid fuels and chemicals. As far as gasification is concerned, the gasifiers can be broadly catalogued into fixed bed,[1] fluidized bed, [2-5] and entrained flow reactors.[6-8] By virtue of higher syngas yield and low-tar product gas, entrained flow reactors have been widely utilized for coal gasification. However, only a few experimental investigations are published on entrained flow biomass gasification. For example, Hernández et al.[6] experimentally studied the effect of the addition of steam to air as gasifying agent in biomass entrained flow gasification and they found that the addition of steam proved positive for the process performance. Qin et al.[8] has experimentally investigated the gasification of two types of biomass, wood and straw, in a laboratory scale atmospheric pressure entrained flow reactor at low oxygen concentration and they found that the biomass was completely converted and the syngas contained nearly no tar at the highest applied reaction temperature of 1350 °C. Besides the few experimental studies, reported works on Computational Fluid Dynamics (CFD) modeling of biomass gasification in entrained flow reactor are not available to our knowledge.

CFD models are powerful predictive tools in multiphase reacting flow research. Generally, all the CFD models developed can be broadly categorized into Eulerian-Eulerian and Eulerian-Lagrangian approaches.

Author's Post-print version. Article published in Energy & Fuels (ACS Publications):
DOI: 10.1021/ef5010557
Published version: https://pubs.acs.org/doi/abs/10.1021/ef5010557

For Eulerian-Eulerian approach, both fluid and particle phases are treated as interpenetrating continua. However, in addition to the difficulty of providing closure models for inter-phase interaction within its continuum framework, Eulerian-Eulerian approach does not recognize the discrete character of the particle phase and thus has trouble in modeling flows with a distribution of particle types and sizes. These difficulties can be naturally overcome by Eulerian-Lagrangian approach in which the gas is treated as continuous and particle as discrete phase. Each particle is tracked in space and time by directly integrating the equations of motion while accounting for interactions with the continuous phase. Eulerian-Lagrangian approach has been widely used to simulate coal combustion or gasification in the last decade.[9-17] However, an Eulerian-Lagrangian model of entrained flow biomass gasification and its validation is not available to our knowledge. Additionally, experimental data available for an actual entrained flow biomass reactor are very limited due to the challenge related to the required high grindability of the fuel and problems with slagging. Yet recently, Qin et al.[7] performed such experiments in a high-temperature (1000-1400°C) lab-scale entrained flow reactor in which biomass particles were injected along with air jets from a central nozzle and steam was injected from the surrounding secondary nozzle hole. They obtained syngas composition measurements at the outlet of the reactor for different operating conditions. Taking into account the literature background, in this paper, we describe the construction of a multi-scale Eulerian-Lagrangian CFD model for a high-temperature biomass entrained flow reactor using the open source code, OpenFOAM (version 2.1.1).[18] All processes of heat and mass transfer, pyrolysis, homogeneous and heterogeneous reactions, radiation, and the interactions between the continuous gas phase and discrete particles have been implemented. Particular emphasis is placed on the effects of five operating parameters (reactor temperature, steam/carbon molar ratio, excess air ratio, biomass type, and particle size) on the gas product composition, syngas yield, particle residence time, and carbon conversion. The predictive capacity and accuracy of the

Author's Post-print version. Article published in Energy & Fuels (ACS Publications):
DOI: 10.1021/ef5010557
Published version: https://pubs.acs.org/doi/abs/10.1021/ef5010557

proposed model is also demonstrated by validating the integrated model against a wide range of experimental data of Qin et al.[7]

2. MATHEMATICAL MODELING

The CFD model is formulated using the Eulerian-Lagrangian frame of reference meaning transport equations are solved for the continuous gas phase and trajectories of discrete particles are tracked through the calculated gas field. The interaction between the continuous phase and the discrete phase is taken into account by treating the exchange of mass, momentum and energy between the two phases as source terms in the governing equations.

2.1. Discrete Particle Phase. The behavior of particles is modeled in a Lagrangian manner. It is assumed that the fuel particles, which consist of a mixture of volatile matter, char and ash, can be represented as spherical particles with a prescribed size distribution. The particles are also subjected to turbulent dispersion which is modeled using a stochastic turbulent dispersion model. The governing mass, momentum, and energy equations for particles are as follows,[14,19]

Mass:

$$\frac{dm_i}{dt} = \frac{dm_{\text{vapor}}}{dt} + \frac{dm_{\text{devol}}}{dt} + \frac{dm_{\text{C-O}_2}}{dt} + \frac{dm_{\text{C-CO}_2}}{dt} + \frac{dm_{\text{C-H}_2\text{O}}}{dt} \quad (1)$$

Momentum:

$$\frac{d\mathbf{v}_i}{dt} = \mathbf{f}_{\text{D},i} + \mathbf{g}\left(1 - \frac{\rho_{\text{g}}}{\rho_i}\right) \quad (2)$$

$$\mathbf{f}_{\text{D},i} = \frac{3\mu_{\text{g}} C_{\text{D}} \,\text{Re}_{\text{p}}}{4\rho_i d_i^2}(\mathbf{u}_{\text{g}} - \mathbf{v}_i) \quad (3)$$

Author's Post-print version. Article published in Energy & Fuels (ACS Publications):
DOI: 10.1021/ef5010557
Published version: https://pubs.acs.org/doi/abs/10.1021/ef5010557

$$C_D = \begin{cases} \frac{24}{Re_p}(1+\frac{1}{6}Re_p^{2/3}) & Re_p \le 1000 \\ 0.424 & Re_p > 1000 \end{cases} \quad (4)$$

$$Re_p = \rho_g d_i \left|\mathbf{u}_g - \mathbf{v}_i\right| / \mu_g \quad (5)$$

Energy:

$$m_i c_i \frac{dT_i}{dt} = h_i A_i (T_g - T_i) + \frac{\varepsilon_i A_{pi}}{4}(G - 4\sigma T_i^4) - H_{evap} dm_{vapor} - H_{O_2/CO_2/H_2O} dm_{C\text{-}O_2/CO_2/H_2O} \quad (6)$$

where m_i, $\mathbf{v}_i$, ρ_i, d_i, c_i, T_i, A_{pi}, and ε_i are, respectively, the mass, velocity, density, diameter, specific heat, temperature, external surface area, and emissivity of particle i, and $\mathbf{g}$ is the gravitational acceleration. ρ_g, $\mathbf{u}_g$, μ_g, and T_g are the density, velocity, dynamic viscosity, and temperature of gas, respectively. $\mathbf{f}_{D,i}$, C_D, and Re_p are the drag per unit mass, drag coefficient, and particle Reynolds number. The choice of drag force models has been discussed in earlier publication.[20] h_i is the inter-phase thermal transfer coefficient, G is the incident radiation whose initial value is set to zero and its transport equation is solved by P-1 radiation model. The P-1 model is the approximate of more general P-N model and has generally been chosen for pulverised fuel combustion and gasification for CFD applications. [17] σ is the Stefan-Boltzmann constant, and H is the heat of reaction to evaporate water (latent heat) or one of the three heterogeneous char reactions. dm_{vapor}, dm_{devol}, $dm_{C\text{-}O2}$, $dm_{C\text{-}CO2}$, and $dm_{C\text{-}H2O}$ are the change in mass of particle i due to loss of water vapor, devolatilization, and char reactions, respectively. As shown in Eq. (6), the particle temperature is calculated taking into account the heat transfer due to convection, radiation, and source terms which includes both the latent heat of vaporization of water from the particle to the gas phase and the heat generated by the heterogeneous char reactions.

2.2. Pyrolysis. The particle phase accounts for fuel conversion via pyrolysis and char consumption. Since

Author's Post-print version. Article published in Energy & Fuels (ACS Publications):
DOI: 10.1021/ef5010557
Published version: https://pubs.acs.org/doi/abs/10.1021/ef5010557

the entrained flow reactor operates at high temperatures, the pyrolysis process occurs at a very fast rate. The pyrolysis compositions released from the fuel can be expressed by the following equilibrium equation and each product yield is solved with the help of the elemental conservation relationships.

$$\text{Biomass} \rightarrow \alpha_1 CO + \alpha_2 H_2O + \alpha_3 CO_2 + \alpha_4 H_2 + \alpha_5 CH_4 + \alpha_6 \text{char (s)} + \alpha_7 \text{ash (s)}, \quad \sum_i \alpha_i = 1 \tag{7}$$

Note that, in the present model, CH_4 is the only hydrocarbon species taken into consideration. Although C_2H_2, C_2H_4, C_2H_6, and other higher hydrocarbons (tar) are produced in the pyrolysis process, they are treated as non-stable products and this mechanism has also been widely used by other researchers.[21,22] Soot is also an increasingly important topic in the field of biomass gasification research but the fundamental aspects of soot have been mainly studied by experiments using lab-scale reactors. Considering there is no simple soot model which can be easily coupled to 3D CFD model, no attempt is made to model soot here. The carbon contained in the fuel which is not converted to CO, CO_2, and CH_4 in the pyrolysis process will be remained in the solid char based on Eq. (7). The heterogeneous reactions, which will be described in more detail in the following subsection, are responsible for the char reactions in the presence of oxygen, carbon dioxide and steam. However, soot will be addressed in the further development of the presented work.

Consistent with Abani and Ghoniem's[9] work, the devolatilization rate is modeled using a single step first-order Arrhenius reaction.

$$\frac{dm_{\text{devol}}}{dt} = -A \exp\left(-\frac{E}{RT_p}\right) m_{\text{devol}} \tag{8}$$

where m_{devol} is the mass of the volatiles remaining in the particle, A=5.0×10^6 s^{-1}, E= 1.2×10^8 J/kmol,[23] and T_p is the particle temperature. The devolatilization process is assumed to be energetically neutral because the

Author's Post-print version. Article published in Energy & Fuels (ACS Publications):
DOI: 10.1021/ef5010557
Published version: https://pubs.acs.org/doi/abs/10.1021/ef5010557

heat of devolatilization is generally negligible as compared to heat of reactions due to char consumption and combustion reactions.[9]

2.3. Char Conversion Chemistry. After devolatilization, the fuel particle is left with char and ash. The ash is assumed to be carried along with the particle, exiting the reactor without taking part in any reactions. Char will react in the presence of oxygen, carbon dioxide and steam and gets converted into carbon monoxide and hydrogen. The following heterogeneous reactions are assumed and implemented in OpenFOAM.

$$C + 0.5O_2 \rightarrow CO \qquad (R1)$$

$$C + CO_2 \rightarrow 2CO \qquad (R2)$$

$$C + H_2O \rightarrow CO + H_2 \qquad (R3)$$

Reaction R1 is the partial oxidation reaction of char which is exothermic. Reactions R2 and R3 are endothermic gasification reactions and R2 is known as Boudouard reaction.

The char consumption rate which includes the effects of both bulk diffusion and chemical reaction rates is given as

$$\frac{dm_{C\text{-}i}}{dt} = -A_p p_{i,g} \frac{r_{diff,i} r_{kin,i}}{r_{diff,i} + r_{kin,i}} \qquad (9)$$

$$r_{diff,i} = \frac{C_i \left[(T_p + T_g)/2 \right]^{0.75}}{d_p} \qquad (10)$$

$$r_{kin,i} = A_i \exp(-\frac{E_i}{RT_p}) \qquad (11)$$

where $m_{C\text{-}i}$ is the mass of the char remaining in the particle when char reacts with gasifying species i (=O_2,

Author's Post-print version. Article published in Energy & Fuels (ACS Publications):
DOI: 10.1021/ef5010557
Published version: https://pubs.acs.org/doi/abs/10.1021/ef5010557

CO_2, or H_2O), A_p is the particle surface area, $p_{i,g}$ is the partial pressure of the gasifying species in the gas surrounding the particle, $r_{diff,i}$ and $r_{kin,i}$ are the diffusion rate and the kinetic rate, respectively. T_p and T_g are particle and gas temperatures, d_p is the particle diameter and C_i is the mass diffusion rate constant. A_i and E_i are the parameters typical of the Arrhenius forms of kinetic rates. For wood biomass considered in the present study, the constants used for kinetic and diffusion rates are assembled in Table 1.[9,24,25]

Table 1

2.4. Continuous Gas Phase. For continuum gas phase, the governing mass, momentum, energy, and species equations can be typically represented by the following equations,[14,26]

Mass:

$$\frac{\partial \rho_g}{\partial t} + \nabla \cdot (\rho_g \mathbf{u}_g) = S_{p,m} \tag{12}$$

Momentum:

$$\frac{\partial}{\partial t}(\rho_g \mathbf{u}_g) + \nabla \cdot (\rho_g \mathbf{u}_g \mathbf{u}_g) = -\nabla p + \nabla \cdot (\boldsymbol{\tau}_{eff}) + \rho_g \mathbf{g} + S_{p,mom} \tag{13}$$

Energy:

$$\frac{\partial}{\partial t}(\rho_g E) + \nabla \cdot (\mathbf{u}_g(\rho_g E + p)) = \nabla \cdot \alpha_{eff} \nabla h_s + S_h + S_{p,h} + S_{rad} \tag{14}$$

$$E = h_s - p/\rho_g + u_g^2/2 \tag{15}$$

Species:

$$\frac{\partial \rho_g Y_i}{\partial t} + \nabla \cdot (\rho_g \mathbf{u}_g Y_i) = \nabla \cdot \rho_g D_{i,eff} \nabla Y + S_{p,Y_i} + S_{Y_i} \tag{16}$$

Author's Post-print version. Article published in Energy & Fuels (ACS Publications):
DOI: 10.1021/ef5010557
Published version: https://pubs.acs.org/doi/abs/10.1021/ef5010557

Here, ρ_g, $\mathbf{u}_g$, p, and h_s are the density, velocity, pressure, and sensible enthalpy of the gas phase, respectively. Y_i is the mass fraction of the *ith* species in the gas mixture. $S_{p,m}$, $S_{p,mom}$, $S_{p,h}$, $S_{p,Yi}$ are the source terms that describe inter-phase exchange terms for mass, momentum, enthalpy and species. S_h and S_{Yi} are the source terms due to the homogeneous gas phase reactions. S_{rad} is the radiation source term. The effective stress tensor, $\boldsymbol{\tau}_{eff}$, is the sum of the viscous and turbulent stresses and calculated as follows,

$$\boldsymbol{\tau}_{eff} = -\frac{2}{3}\mu_{eff}(\nabla \cdot \mathbf{u}_g)\mathbf{I} + \mu_{eff}((\nabla \mathbf{u}_g) + (\nabla \mathbf{u}_g)^T) \quad (17)$$

where effective dynamic viscosity $\mu_{eff} = \mu_g + \mu_t$. μ_g is gas phase viscosity, μ_t is turbulent viscosity and will be described in more detail below. Similarly the effective dynamic thermal diffusivity α_{eff} and mass diffusion coefficient for species D_{eff} also take both the viscous and turbulent contributions into account.

$$\alpha_{eff} = \alpha_g + \frac{\mu_t}{Pr_t} \quad (18)$$

$$D_{eff} = D_g + \frac{\mu_t}{\rho_g Sc_t} \quad (19)$$

here α_g and D_g are gas phase thermal diffusivity and the mass diffusion coefficient for species in the mixture, respectively. As shown by Eqs. (18) and (19), the turbulent thermal diffusivity and turbulent mass diffusion coefficient are calculated using a turbulent Prandtl number (Pr_t) and a turbulent Schmidt number (Sc_t), respectively. In our model we assume that Pr_t=1.0 and Sc_t=1.0 which are standard values used in OpenFOAM.

There are big variations in the gas velocity within the reactor due to large temperature gradients and a large amount of gas products from biomass by devolatilization and gasification. Hence the local Reynolds number can be very high and turbulence should be taken into account. In order to resolve turbulence, the

Author's Post-print version. Article published in Energy & Fuels (ACS Publications):
DOI: 10.1021/ef5010557
Published version: https://pubs.acs.org/doi/abs/10.1021/ef5010557

governing transport equations for k and ε is solved and it is the most frequently employed turbulence model in CFD studies of gasification.[14]

$$\frac{\partial}{\partial t}(\rho_g k) + \nabla \cdot (\rho_g \mathbf{u}_g k) = \nabla \cdot \left(\left(\mu_g + \frac{\mu_t}{\sigma_k} \right) \nabla k \right) + G_k - \rho_g \varepsilon \quad (20)$$

$$\frac{\partial}{\partial t}(\rho_g \varepsilon) + \nabla \cdot (\rho_g \mathbf{u}_g \varepsilon) = \nabla \cdot \left(\left(\mu_g + \frac{\mu_t}{\sigma_\varepsilon} \right) \nabla \varepsilon \right) + \frac{\varepsilon}{k}(C_{\varepsilon 1} G_k - C_{\varepsilon 2} \rho_g \varepsilon) \quad (21)$$

Here k is the turbulent kinetic energy, ε is the dissipation rate of turbulent kinetic energy, and G_k represents the generation term for k. The constants $C_{\varepsilon 1}$=1.44, $C_{\varepsilon 2}$=1.92, σ_k=1.0, and σ_ε=1.3. μ_t is the gas phase turbulent viscosity which is computed as a function of k and ε,

$$\mu_t = \rho_g C_\mu \frac{k^2}{\varepsilon} \quad (22)$$

where C_μ is a constant which is set as 0.09 as standard.

2.5. Gas Phase Reactions. Simple global reactions are used to describe the gas phase chemistry and the effect of turbulence on combustion and gasification is resolved by the partially stirred reactor (PaSR) model.[9] Chemical reaction equations and their kinetic constants as well as adopted references are shown in Table 2. Reactions R4 and R5 are the consumption of CH_4 through oxidation and steam reactions. Reactions R6 and R7 are H_2 and CO consumption reactions. Reaction R8 is known as the reversible water-gas shift reaction and the forward reaction rate k_f and backward reaction rate k_b are related by the equilibrium constant $k_{eq}=k_f/k_b$.

Table 2

2.6. Computational Methodology. Since the governing equations for particles and the gas phase are

Author's Post-print version. Article published in Energy & Fuels (ACS Publications):
DOI: 10.1021/ef5010557
Published version: https://pubs.acs.org/doi/abs/10.1021/ef5010557

different, different solution schemes have to be used. For discrete particles, a first-order Euler time integration scheme is used to solve the particle motions. Meanwhile, the drying, pyrolysis, and gasification submodels update particle properties like temperature, composition, and heat capacity at each fluid time step. For continuous gas phase, time discretization of the transporting equations is based on an Euler scheme and spatial discretization uses a finite-volume technique. The coupling between the discrete particles and the gas phase is achieved by the inter-phase source terms ($S_{p,m}$, $S_{p,mom}$, $S_{p,h}$, $S_{p,Yi}$), which are solved at every fluid time step. All mathematical models and schemes described above have been developed and implemented into an open source C++ toolbox OpenFOAM (OpenCFD Ltd, 2012).

3. SIMULATION SETUP

Figure 1

Figure 2

The simulations are performed on the Technical University of Denmark (DTU) lab-scale entrained flow reactor which operates at atmospheric pressure, with a length of 202 cm and a diameter of 8 cm. A schematic of experimental setup is shown in Figure 1 and a more detailed description of the experimental facility can be found in the literature.[7] Here, the reaction tube is constructed and meshed using OpenFOAM preprocessing utility. A three-dimensional structured grid consisting of 281280 cells is employed to define the total volume and is depicted in Figure 2(a). The mesh is locally refined in the center injection zone in order to enhance the prediction of the devolatilization and initial combustion steps of the fuel particles. Figure 2(b) shows the top view of the reactor inlet which consists of a center inlet and a concentric ring inlet. Four common biomasses in Europe[2,7] are used as the fuel and their properties, such as proximate and elemental analyses, are summarized in Table 3. The compositions of volatiles for the four biomasses, which

Author's Post-print version. Article published in Energy & Fuels (ACS Publications):
DOI: 10.1021/ef5010557
Published version: https://pubs.acs.org/doi/abs/10.1021/ef5010557

are shown in Table 4, are determined by the equilibrium equation (Eq.7) and the elemental conservation relationships. The volatiles are a mixture of H_2, CO, CO_2 and CH_4. Because of high temperatures encountered in the entrained flow reactor, the volatiles release at a very fast rate which is calculated from Eq. (8). When the compositions of volatiles are released from the fuel particles, their combustion and gasification are naturally taken into account by the homogeneous reactions listed in Table 2.

Table 3

Table 4

The grid resolution employed here is arrived at by a corresponding grid independence study. To seek a proper grid system, four different grid systems of 70320 cells, 140640 cells, 281280 cells, and 351600 cells are tested. In the test, only air (293 K) with the uniform inlet velocity (U_0) is injected into the reactor. Figure 3 displays the U_z velocity distribution in the mid plane and at the bottom exit of the reactor. It can be seen that the velocity profiles in terms of the third and fourth grid systems coincide with the analytic solution. This implies that the third grid system of 281280 cells can satisfy the requirement of grid independence. Note that for turbulent multiphase reacting flows, the choice of grid size is somewhat not straightforward. Kumar and Ghoniem (2012)[14] concluded that it became increasingly difficult to find a steady-state solution for a very finer mesh due to the inherently transient problem of turbulent multiphase reacting flows in gasifiers and the stochastic nature of the particle turbulent dispersion model. Therefore, the grid system of 281280 cells is a good choice which takes both the grid independence and steady-state solution into account.

Figure 3

Biomass is fed into the reactor from the center inlet by the cold feeder air stream (10 Nl/min). Both the

Author's Post-print version. Article published in Energy & Fuels (ACS Publications):
DOI: 10.1021/ef5010557
Published version: https://pubs.acs.org/doi/abs/10.1021/ef5010557

biomass and feeder air temperatures are 300 K. The preheated air and steam, whose temperatures are equal to the operating temperature, are blown into the reactor from the outer ring inlet. The fuel particles are injected using a stochastic technique and at the rate of 50,000 particles per second. Four mean particle diameters ($\bar{d}_p$ = 200, 310, 500, 750 μm) are employed to study the effect of particle size and the initial particle size distributions follow the Rossin-Rammler distribution which are shown in Figure 4. The particle size distributions are the same for all the biomasses studied. Initially a pure nitrogen environment within the reactor is adopted, i.e., at the start of simulation (t = 0), there is only one species (N_2) in the reactor. The operation conditions are established using measurements made during the experimental runs[7] and the detailed test cases are listed in Table 5. As shown in Table 5, besides 27 gasification cases, we have also tested three pyrolysis cases.

Figure 4

Table 5

4. RESULTS AND DISCUSSIONS

In the following subsections, the productions of the main gas product components (H_2, CO, CO_2, and CH_4, expressed in Nm^3 of gas component produced per kg of dry and ash-free fuel) is used to explore the effects of different operating conditions on pyrolysis and gasification performances. The gas production can provide valuable information on the overall gasification process, since it takes into account both the gas quality and the fuel conversion.

4.1. Pyrolysis. Compared to coal, biomass typically has much higher volatile matter content. For the four biomasses studied, the volatile content is more than 70% (see Table 3). Therefore, the pyrolysis process is

Author's Post-print version. Article published in Energy & Fuels (ACS Publications):
DOI: 10.1021/ef5010557
Published version: https://pubs.acs.org/doi/abs/10.1021/ef5010557

more important for biomass than coal. In this subsection we first validate our integrated CFD model by testing three pyrolysis cases. The corresponding experimental runs are conducted by Qin et al. [7] For pyrolysis cases, 10 Nl/min N_2 is employed as feeder gas which is different from the 10 Nl/min air stream used for gasification cases.

Figure 5

Figure 5 shows the species production in the product gas for the three pyrolysis cases (cases P1-P3 in Table 5) and the predicted results are compared with experimental data reported by Qin et al.[7] The lines represent the numerically calculated results, whereas the corresponding symbols represent the experimental data. Note that the hydrocarbon production in the experimental work of Qin et al.[7] are joined together as CH_4. It can be seen that the predictions of the model show good conformance to the experimental measurements. For H_2, the minimum relative error of calculation to experiment is about 5% and the maximum relative error is less than 15%. For CO, the minimum relative error is about 1% and the maximum relative error is less than 9%. For CO_2, the minimum relative error is about 3% and the maximum relative error is within 22%. The errors of CH_4 are somewhat large, which might relate to its small amounts which are easily to cause big errors. However, considering the simple single step first-order Arrhenius reaction equation (Eq. 8) used for modeling pyrolysis process in our CFD model, the match between our predictions and experimental results of Qin et al.[7] can be considered encouraging.

Figure 6

Figure 6 shows the predicted averaged particle residence time along the reactor length for the three pyrolysis cases (cases P1-P3 in Table 5). It is observed that a higher S/C ratio results in a shorter particle residence time inside the reactor. This is reasonable since the steam flow rate increases with an increase in

Author's Post-print version. Article published in Energy & Fuels (ACS Publications):
DOI: 10.1021/ef5010557
Published version: https://pubs.acs.org/doi/abs/10.1021/ef5010557

the S/C ratio causing a decrease in the particle residence time. In addition, the particle residence times at the outlet of the reactor are summarized in Table 5.

Figure 7

Figure 7 depicts the averaged particle weight loss along the reactor length for case P1. It is easily seen that the volatiles releases at a very fast rate and the devolatilization is finished just downstream the inlet (z = 0.2). Moreover, from Figure 6, we can extract that at z = 0.2 the predicted particle residence time for case P1 is 0.16 s.

The above subsection has shown the validity of the integrated CFD model by comparing our simulated results for pyrolysis cases with the experimental data obtained from the literature.[7] In the following, the proposed model is further validated by testing a wide range of gasification cases.

4.2. Gasification Phenomena. Some qualitative results are firstly presented. Figure 8(a) shows the predicted temperature contours in the mid plane of the reactor at T_r = 1400 °C, S/C=0.5, and λ = 0.3 for Beech wood (case G5 in Table 5). It is clearly observed that the peak temperature (around 2200 K) exists away from the axis, in a region just following the fuel injection. The sharp temperature increase near the injector is owing to the exothermic combustion of volatiles as more than 75% of the Beech wood injected is devolatilized and transported radially outward from the cold central jet, along with the conveyance air fed from the inlets. This is typical of jet diffusion flames.[9] Further downstream the temperature distribution is nearly homogeneous and gasification reactions are dominant. Figure 8(b-g) present the concentration (mass fraction) contours of gas phase species in a plane passing through the axis of the reactor. A higher concentration of H_2, CO, CO_2, and CH_4 in the upstream region can be explained due to the volatile matter content of wood, which releases high amount of volatiles during devolatilization. Figure 8(g) demonstrates

Author's Post-print version. Article published in Energy & Fuels (ACS Publications):
DOI: 10.1021/ef5010557
Published version: https://pubs.acs.org/doi/abs/10.1021/ef5010557

that the oxygen is quickly consumed during the combustion of volatiles. In the downstream CO and H_2 concentrations are higher and CO_2 and H_2O concentrations are lower, which are attributed to the char gasification reactions. Figure 8(h) shows the biomass particle distribution colored according to the char concentration (mass fraction) remaining in the particle. It can be seen that, just downstream the inlet, the particle has some volatiles left and hence, the mass fraction of char is low (blue color). After a fast devolatilization, the particles have higher char concentration (red color) because there are only char and ash left. In the further downstream, the char gets consumed and most of the particles have low concentration of char (blue color) because they are left with only ash. Figure 8(i) plots the corresponding char burnout rate of each particle. It can be observed that, just downstream of the inlet, the char burning rate is high due to the existence of oxygen in this location. Further downstream, most of the particles are gone with only ash remaining as shown in Figure 8(h) and therefore they have zero char burnout rate. The predicted char conversion from simulation for this case is 95.8% which is in good agreement with the measured value about 93% reported by Qin et al.[7]

Figure 8

4.3. Effect of Reactor Temperature. In this subsection the effect of the reactor temperature on the species production and particle residence time is studied. Reactor temperature (T_r, defined as the external temperature of the reactor tube) ranges from 1000 to 1400 °C with otherwise fixed operating parameters (cases G1-G5 in Table 5). Figure 9 compares the predicted results with experimental data reported by Qin et al.[7] Again, the predictions of the model show good conformance to the experimental measurements. For the two most important syngas species (H_2, CO), the minimum relative error of calculation to experiment is about 1% and the maximum relative error is less than 25%. For CO_2, the minimum relative error is about 0.5%

Author's Post-print version. Article published in Energy & Fuels (ACS Publications):
DOI: 10.1021/ef5010557
Published version: https://pubs.acs.org/doi/abs/10.1021/ef5010557

and the maximum relative error is less than 6%. For CH_4, the maximum relative error is also within 19%. The over-estimation of H_2 can probably be attributed to the neglect of tar and methanation reaction.

Figure 9

Figure 10 shows the predicted averaged particle residence time along the reactor length for different reactor temperatures. It is easily seen that an increase in T_r will decrease the particle residence time inside the reactor and this trend is qualitatively consistent with the experimental findings of Qin et al. [7] However, here we will not attempt to quantitatively compare our predicted particle residence times with those of Qin et al. [7] The particle residence times of our simulation are directly calculated from the residence time of each particle, whereas the particle residence times of Qin et al.[7] were approximately estimated by the gas mean residence time assuming that there was no relative velocity between the solid phase and gas phase. This is strictly speaking not necessarily the case and new advanced experimental techniques are needed in order to accurately measure the particle residence time as comparison to the CFD.

Figure 10

Both the reactor temperature and the particle residence time have important roles for the reaction progress. Although the particle residence time is shorter at higher reactor temperatures as shown in Figure 10, the reactor temperature has a more significant effect on the increase in the reaction rate. It means that, within the T_r range studied (1000-1400 °C), the increase in the reactor temperature is dominant for determining the gas composition. As shown in Figure 9, rising temperature leads to a substantial increase in the H_2 and CO productions which are due to two reasons: (i) the production of H_2 and CO through the endothermic char gasification reactions (R2, R3), which are favorable at elevated temperatures, and (ii) the increase of H_2 and CO yield resulting from the steam reforming of CH_4 (R5). Simultaneously, the CO_2 production

Author's Post-print version. Article published in Energy & Fuels (ACS Publications):
DOI: 10.1021/ef5010557
Published version: https://pubs.acs.org/doi/abs/10.1021/ef5010557

monotonically decreases with increasing temperature because of its consumption via Boudouard reaction (R2, promoted at higher temperatures), and the CH_4 yield also declines steadily with the rise in temperature and nearly vanishes at 1400°C due to the steam reforming reaction (R5).

4.4. Effect of Steam/Carbon Molar Ratio. In this subsection the effect of the steam/carbon molar ratio (denoted by S/C) on species production and particle residence time is explored. Accordingly, three different cases (cases G6-G8 in Table 5) where the S/C ratio varies from 0 to 1.0 with otherwise fixed operating parameters are tested. Figure 11(a) shows the productions of the main components in the product gas as a function of S/C ratio. Note that the yield of CH_4 is fairly low in contrast to the other species at T=1400 °C (see Figure 9) so that it is not shown in this figure. Again, the calculated results show a good agreement with the experimental measurements. For H_2 and CO, the minimum relative error of calculation to experiment is about 4% and the maximum relative error is less than 19%. For CO_2, the minimum relative error is about 5% and the maximum relative error is also within 19%. It can be also easily observed that the H_2 and CO_2 productions increase steadily while the CO yield decreases almost linearly by increasing the steam/carbon ratio. These results can be explained mainly by the water-gas shift reaction (R8) which transforms CO and steam to H_2 and CO_2. As the S/C ratio increases, the partial pressure of steam and the steam flow rate increases. It means that the rate of the water-gas shift reaction (R8) increases. Figure 11(b) plots the H_2/CO molar ratio in the product gas as a function of S/C ratio. The increase of H_2/CO ratio from about 0.7 (S/C=0) to about 1.1 (S/C=1) confirms the promotion of the water-gas shift reaction due to the increase of the available steam to get involved in the reaction.

Figure 11

Figure 12 shows the predicted averaged particle residence time along the reactor length for different S/C

Author's Post-print version. Article published in Energy & Fuels (ACS Publications):
DOI: 10.1021/ef5010557
Published version: https://pubs.acs.org/doi/abs/10.1021/ef5010557

ratios. As expected, an increase in S/C ratio will decrease the particle residence time inside the reactor since the S/C ratio is controlled by the steam flow rate which increases with the S/C ratio. For the narrow S/C ratio range studied (0-1.0), the increase in the reaction rate of water-gas shift reaction (R8) has more significant effect than the decrease in the particle residence time.

Figure 12

4.5. Effect of Excess Air Ratio. The excess air ratio, λ, is ratio of net air input in the reactor to the amount of stoichiometric air needed for complete combustion of the fuel. λ could be varied either by changing the fuel feeding flow rate while keeping the air flow constant or vice versa. In this subsection, the total inlet air rate is kept constant and the applied excess air ratio is increased from 0.25 to 0.35 by lowering the fuel feeding rate with otherwise fixed operating parameters (cases G9-G11 in Table 5). Figure 13 presents the effect of λ on the species production. For H_2 and CO, the minimum relative error of calculation to experiment is about 3% and the maximum relative error is less than 18%. For CO_2, the maximum relative error is within 9%. It is also found that increasing λ clearly decreases the H_2 and CO productions but increases the CO_2 production. These trends are most likely because of more oxidizing conditions at the higher excess air ratio, leading to oxidation of H_2 and CO (R6, R7).

Figure 13

Figure 14 shows the predicted averaged particle residence time along the reactor length for different excess air ratios λ. It is observed that an increase in λ will increase the particle residence time inside the reactor and this trend is also qualitatively consistent with the experimental findings of Qin et al. [7]

Figure 14

Author's Post-print version. Article published in Energy & Fuels (ACS Publications):
DOI: 10.1021/ef5010557
Published version: https://pubs.acs.org/doi/abs/10.1021/ef5010557

The above subsections have demonstrated the validity of the integrated CFD model by comparing our simulated results for both pyrolysis and gasification cases with the wide range of experimental data of Qin et al. [7] In the following, in order to further demonstrate the *predictive* capacity of the proposed model, the calculated results are used to explore the effects of biomass type and particle size on gasification performance for which we have not been able to find suitable experimental data for.

4.6. Effect of Biomass Type. Four common biomasses in Europe (Beech, Pine, Holm-oak, Eucalyptus) are adopted to explore the effect of biomass type on gasification behavior (cases G12-G15 in Table 5). Beech, Holm-oak and Eucalyptus are hardwood, while Pine is softwood. Figure 15 shows the predicted temperature contours, mass fraction distributions of H_2 and CO in the mid plane of the reactor, and fuel particle distributions colored according to the char concentration remaining in the particle for the four biomasses. It is seen that, regardless of which biomass is consumed, the peak temperature (around 2200 K) always exists away from the axis, in a region just following the fuel injection (Figure 15a). The sharp temperature increase near the injector is owing to the exothermic combustion of volatiles. At the exit, the concentrations of H_2 from the gasification of Beech and Eucalyptus are relatively higher, whereas the concentration of CO from the gasification of Holm-oak is the lowest (Figure 15bc). Figure 15 overally indicates that the gasification phenomenon is qualitatively similar for the four biomasses, and there is no significant difference in the contours which can be attributed to their similar properties as shown in Table 3 (high volatile matter, low ash and high oxygen).

Figure 15

Figure 16 presents the species production at the reactor exit for the four biomasses. It is observed that,

Author's Post-print version. Article published in Energy & Fuels (ACS Publications):
DOI: 10.1021/ef5010557
Published version: https://pubs.acs.org/doi/abs/10.1021/ef5010557

1 although the Beech and Eucalyptus exhibit higher H_2 production and the Holm-oak gets a lowest CO
2 production, the four biomasses generally provide quite similar gasification performance with little difference
3 in the species productions. This finding is qualitatively consistent with the results of previous experimental
4 studies.[2,7] Therefore, one biomass can be replaced by another without any major consequences in the process
5 performance. This is advantageous, because the availability of biomass fuel is very seasonal.

6 Figure 16

7 Carbon conversion (CC) is another vital index used for evaluating the performance of gasification. It is
8 defined as follows:[29]

9 $$\mathrm{CC}(\%) = \frac{\dot{m}_{\mathrm{out,CO}} 12/28 + \dot{m}_{\mathrm{out,CO_2}} 12/44 + \dot{m}_{\mathrm{out,CH_4}} 12/16}{\dot{m}_{\mathrm{in,fuel}} Y_{\mathrm{c}}} \times 100 \quad (23)$$

10 where Y_c is the mass fraction of carbon in the feed fuel.

11 Figure 17

12 Figure 17 shows the predicted CC at the reactor exit for the four biomasses. Specifically, the values of CC
13 for the Beech, Pine, Holm-oak, and Eucalyptus are 95.8%, 97.3%, 91.1%, and 94.0%, respectively, revealing
14 that over 90% of the carbon in these fuels is converted to CO, CO_2, and CH_4 because of high operating
15 temperature (1400 °C). Figure 18 depicts the predicted averaged particle residence time along the reactor
16 length for different biomasses. As expected, the Pine (softwood) has the longest residence time because of its
17 lower density compared to other biomasses (hardwood), which is probably why Pine has the highest carbon
18 conversion (97.3%).

19 Figure 18

Author's Post-print version. Article published in Energy & Fuels (ACS Publications):
DOI: 10.1021/ef5010557
Published version: https://pubs.acs.org/doi/abs/10.1021/ef5010557

4.7. Effect of Particle Size. Four mean particle diameters ($\bar{d}_p$=200, 310, 500, 750 μm) are employed to study the effect of particle size on the species production and carbon conversion (cases G12-G27 in Table 5). Figure 19 shows the effect of $\bar{d}_p$ on exit species production for the four biomasses. Overall, the predicted CO and H_2 productions decrease with increasing $\bar{d}_p$, so a smaller particle is conducive to CO and H_2 formation. It is also found that increasing $\bar{d}_p$ leads to very little change in the CO_2 production.

Figure 19

Figure 20

The relation between the carbon conversion and $\bar{d}_p$ is drawn in Figure 20. The symbols represent the 16 simulation cases (cases G12-G27 in Table 5), and the lines almost threading the symbols represent the corresponding fit curves. As indicated, CC decreases with an increasing in $\bar{d}_p$ for all the biomasses studied. In order to explore the possible reasons, Figure 21 depicts the predicted averaged particle residence time along the reactor length at different $\bar{d}_p$ for pine (cases G13, G17, G21, and G25 in Table 5). It is easily observed that smaller particles have a relatively longer residence time as compared to bigger particles and this trend is same for all the four biomasses. This is reasonable because bigger particles have larger inertia and tend to locate near the central fuel jet region. Meanwhile, smaller particles could be easily transported radially toward the walls where the velocity of the carrier gas is lower causing smaller particles to have a longer residence time.

Figure 21

In examining the fit curves shown in Figure 20, the carbon conversions for the Beech, Pine, Holm-oak, and Eucalyptus decreases as the -0.0581, -0.0544, -0.0691, and -0.0754 power of increasing $\bar{d}_p$,

Author's Post-print version. Article published in Energy & Fuels (ACS Publications):
DOI: 10.1021/ef5010557
Published version: https://pubs.acs.org/doi/abs/10.1021/ef5010557

respectively. Note that carbon conversion is accomplished by devolatilization and char heterogeneous reactions in the reactor. The devolatilization of biomass is assumed to be independent of particle diameter (see Eq. 8). The char heterogeneous reactions at high temperature are thought to be inversely proportional to particle diameter for bulk diffusion control.[11] The predicted particle diameter dependences (-0.0581, -0.0544, -0.0691, and -0.0754 powers) fall between the limits for diffusion-controlled heterogeneous reaction (-1 power) and devolatilization (0 power). They are larger than the reported value of -0.145 found by Chen et al.[11] for an entrained flow coal gasifier, because of a much higher volatile matter content of biomass compared to coal.

5. CONCLUSION

A multi-scale Eulerian-Lagrangian CFD model based on OpenFOAM has been constructed, validated and applied to a lab-scale biomass entrained flow reactor. The operating temperatures are high (1000-1400 °C) and effects of five operating parameters (reactor temperature, steam/carbon molar ratio, excess air ratio, biomass type, and particle size) on the species production, particle residence time and carbon conversion are particularly addressed. Results show that the reactor temperature has a positive effect on the quality of the product gas and rising temperature leads to a substantial increase in the H_2 and CO productions; increasing the steam/carbon ratio increases the H_2 production but decreases the CO production; increasing the excess air ratio decreases both the H_2 and CO productions; the biomass type appears to have influence on the gasification behavior to some extent because it results in variations in species production and carbon conversion. However, the variations are not so significant due to similar biomass nature and hence one type can be replaced by another without any major consequences in the gasification performance; and both the CO and H_2 productions and carbon conversion decrease with an increase in particle size for all the biomasses.

Author's Post-print version. Article published in Energy & Fuels (ACS Publications):
DOI: 10.1021/ef5010557
Published version: https://pubs.acs.org/doi/abs/10.1021/ef5010557

Moreover, the predicted results follow the same trends as the wide range of experimental data for both pyrolysis and gasification experiments obtained from the literature.[7] Quantitative comparisons are also made and the agreement is good. Therefore, the established numerical models and chemical kinetics are suitable for simulating wood gasification in high-temperature entrained flow reactor.

■ AUTHOR INFORMATION

Corresponding Author

*Telephone: +47 73593919. Fax: . E-mail: xiaoke.ku@ntnu.no

Notes

The authors declare no competing financial interest.

■ ACKNOWLEDGEMENTS

The authors would like to thank partners in CenBio, the BioEnergy Innovation Centre, and GasBio for financial support.

■ REFERENCES

(1) Umeki, K.; Yamamoto, K.; Namioka, T.; Yoshikawa, K. *Appl. Energ.* **2010**, *87*, 791-798.

(2) Franco, C.; Pinto, F.; Gulyurtlu, I.; Cabrita, I. *Fuel* **2003**, *82*, 835-842.

(3) Li, X. T.; Grace, J. R.; Lim, C. J.; Watkinson, A. P.; Chen, H. P.; Kim, J. R. *Biomass Bioenerg.* **2004**, *26*, 171-193.

(4) Meng, X.; de Jong, W.; Fu, N.; Verkooijen, A. H. M. *Biomass Bioenerg.* **2011**, *35*, 2910-2924.

Author's Post-print version. Article published in Energy & Fuels (ACS Publications):
DOI: 10.1021/ef5010557
Published version: https://pubs.acs.org/doi/abs/10.1021/ef5010557

(5) Song, T.; Wu, J.; Shen, L.; Xiao, J. *Biomass Bioenerg.* **2012**, *36*, 258-267.

(6) Hernández, J.J.; Aranda, G.; Barba, J.; Mendoza, J. M. *Fuel Process Technol.* **2012**, *99*, 43-55.

(7) Qin, K.; Jensen, P. A.; Lin, W.; Jensen, A. D. *Energy Fuels* **2012**, *26*, 5992-6002.

(8) Qin, K.; Lin, W.; Jensen, P. A.; Jensen, A. D. *Fuel* **2012**, *93*, 589-600.

(9) Abani, N.; Ghoniem, A. F. *Fuel* **2013**, *104*, 664-680.

(10) Backreedy, R. I.; Fletcher, L. M.; Ma, L.; Pourkashanian, M.; Williams, A. Combust. Sci. Technol. **2006**, *178*, 763-787.

(11) Chen, C.; Horio, M.; Kojima, T. *Chem. Eng. Sci.* **2000**, *55*, 3875-3883.

(12) Chen, C.; Hung, C.; Chen, W. *Appl. Energ.* **2012**, *100*, 218-228.

(13) Kumar, M.; Ghoniem, A. F. *Energy Fuels* **2012**, *26*, 451-463.

(14) Kumar, M.; Ghoniem, A. F. *Energy Fuels* **2012**, *26*, 464-479.

(15) Silaen, A.; Wang, T. *Int. J. Heat Mass Tran.* **2010**, *53*, 2074-2091.

(16) Watanabe, H.; Otaka, M. *Fuel* **2006**, *85*, 1935-1943.

(17) Álvarez, L.; Gharebaghi, M.; Pourkashanian, M.; Williams, A.; Riaza, J.; Pevida, C.; et al. *Fuel Process. Technol.* **2011,** *92*, 1489-1497.

(18) OpenFOAM Documentation, **2012**. http://www.openfoam.org/docs/.

(19) Liu, A. B.; Mather, D.; Reitz, R. D. *SAE Technical Paper Series* **1993**, 930072.

(20) Ku, X.; Li, T.; Løvås, T. *Chem. Eng. Sci.* **2013**, *95*, 94-106.

Author's Post-print version. Article published in Energy & Fuels (ACS Publications):
DOI: 10.1021/ef5010557
Published version: https://pubs.acs.org/doi/abs/10.1021/ef5010557

(21) Ergüdenler, A.; Ghaly, A. E.; Hamdullahpur, F.; Al-Taweel, A. M. *Energ. Source.* **1997**, *19*, 1065-1084.

(22) Gerber, S.; Behrendt, F.; Oevermann, M. *Fuel* **2010**, *89*, 2903-2917.

(23) Prakash, N.; Karunanithi, T. *J. Appl. Sci. Res.* **2008**, *4*, 1627-1636.

(24) Evans, D. D.; Emmons, H. W. *Fire Res.* **1977**, *1*, 57-66.

(25) Klose, W.; Wölki, M. *Fuel* 2**005**, *84*, 885-892.

(26) Marzouk, O. A.; Huckaby, E. D. *Eng. App. Comput. Fluid Mech.* **2010**, *4*, 331-356.

(27) Gómez-Barea, A.; Leckner, B. *Prog. Energ. Combust.* **2010**, *36*, 444-509.

(28) Jones, W. P.; Lindstedt, R. P. *Combust. Flame* **1988**, *73*, 233-249.

(29) Chen, W.; Chen, C.; Hung, C.; Shen, C.; Hsu, H. *Appl. Energ.* **2013**, *112*, 421-430.

Author's Post-print version. Article published in Energy & Fuels (ACS Publications):
DOI: 10.1021/ef5010557
Published version: https://pubs.acs.org/doi/abs/10.1021/ef5010557

1 **Tables**

2

3 **Table 1. Heterogeneous reaction constants**

Parameters	Values
A_{O2} (s m^{-1})	2.51×10^{-3}
E_{O2} (J $kmol^{-1}$)	7.48×10^{7}
A_{H2O} (s m^{-1})	2.0×10^{-3}
E_{H2O} (J $kmol^{-1}$)	1.96×10^{8}
A_{CO2} (s m^{-1})	3.0×10^{-1}
E_{CO2} (J $kmol^{-1}$)	2.0×10^{8}
C_i ($_i$=O_2, H_2O, CO_2) (s $K^{-0.75}$)	5.0×10^{-12}

4

5

Author's Post-print version. Article published in Energy & Fuels (ACS Publications):
DOI: 10.1021/ef5010557
Published version: https://pubs.acs.org/doi/abs/10.1021/ef5010557

1 **Table 2. Considered chemical reactions and their reaction rates**

Reactions		Reaction rate	Refs
$CH_4 + 2O_2 \rightarrow CO_2 + 2H_2O$	(R4)	$k = 5.16\times10^{13} T^{-1}[CH_4][O_2]\exp(-1.30\times10^{8}/RT)$	27
$CH_4 + H_2O \rightarrow CO + 3H_2$	(R5)	$k = 7.0\times10^{6}[CH_4][H_2O]\exp(-1.26\times10^{8}/RT)$	28
$H_2 + 0.5O_2 \rightarrow H_2O$	(R6)	$k = 2.2\times10^{9}[H_2][O_2]\exp(-1.09\times10^{8}/RT)$	27
$CO + 0.5O_2 \rightarrow CO_2$	(R7)	$k = 1.0\times10^{10}[CO][O_2]^{0.5}[H_2O]^{0.5}\exp(-1.26\times10^{8}/RT)$	27
$CO + H_2O \leftrightarrow CO_2 + H_2$	(R8)	$k_f = 2.78\times10^{3}[CO][H_2O]\exp(-1.26\times10^{7}/RT)$ $k_b = 9.59\times10^{4}[CO_2][H_2]\exp(-4.66\times10^{7}/RT)$ $k_{eq} = 0.029\exp(3.40\times10^{7}/RT)$	27

2

3

Author's Post-print version. Article published in Energy & Fuels (ACS Publications):
DOI: 10.1021/ef5010557
Published version: https://pubs.acs.org/doi/abs/10.1021/ef5010557

1 **Table 3. Biomass properties**

	Beech	Pine	Holm-oak	Eucalyptus
Proximate analysis (wt%, on the as-received basis)				
Moisture	9.04	12.0	9.5	10.6
Ash	0.61	0.5	2.5	0.7
Volatile	76.70	71.5	70.2	74.8
Fixed carbon	13.65	16.0	17.8	13.9
Elemental analysis (wt%, on the daf basis)				
C	49.9	51.6	51.1	52.8
H	6.4	4.9	5.3	6.4
O	43.6	42.6	42.7	40.4
Others	0.1	0.9	0.9	0.4

2

Author's Post-print version. Article published in Energy & Fuels (ACS Publications):
DOI: 10.1021/ef5010557
Published version: https://pubs.acs.org/doi/abs/10.1021/ef5010557

1 **Table 4. Composition of volatile matter for the four biomasses**

	Beech	Pine	Holm-oak	Eucalyptus
Component	*Mass fraction (%)*			
CH_4	18.2	17.8	14.8	24.6
H_2	2.9	1.5	3.0	1.5
CO_2	41.4	42.4	43.8	37.5
CO	37.5	38.3	38.4	36.4

2

Author's Post-print version. Article published in Energy & Fuels (ACS Publications):
DOI: 10.1021/ef5010557
Published version: https://pubs.acs.org/doi/abs/10.1021/ef5010557

Table 5. Test cases

Pyrolysis cases									
Parameter	Case	T_r (°C)	S/C (-)	λ (-)	Fuel (-)	$\bar{d}_p$ (μm)	Fuel feeding rate (g/min)	Particle residence time (s)	Air/Steam flow rates through outer ring inlet (g/min)
Steam/carbon molar ratio (S/C)	P1	1400	0	0	Beech	310	12.8	2.27	0/0
	P2	1400	0.5	0	Beech	310	12.8	1.82	0/4.3
	P3	1400	1.0	0	Beech	310	12.8	1.53	0/8.6
Gasification cases									
Parameter	Case	T_r (°C)	S/C (-)	λ (-)	Fuel (-)	$\bar{d}_p$ (μm)	Fuel feeding rate (g/min)	Particle residence time (s)	Air/Steam flow rates through outer ring inlet (g/min)
Reactor temperature (T_r)	G1	1000	0.5	0.3	Beech	310	12.8	2.55	6.9/4.3
	G2	1100	0.5	0.3	Beech	310	12.8	2.27	6.9/4.3
	G3	1200	0.5	0.3	Beech	310	12.8	2.03	6.9/4.3
	G4	1300	0.5	0.3	Beech	310	12.8	1.80	6.9/4.3
	G5	1400	0.5	0.3	Beech	310	12.8	1.63	6.9/4.3
Steam/carbon molar ratio (S/C)	G6	1400	0	0.3	Beech	310	12.8	1.94	6.9/0
	G7[a]	1400	0.5	0.3	Beech	310	12.8	1.63	6.9/4.3
	G8	1400	1.0	0.3	Beech	310	12.8	1.42	6.9/8.6
Excess air ratio (λ)	G9	1400	0.5	0.25	Beech	310	15.3	1.48	6.9/5.2
	G10[a]	1400	0.5	0.3	Beech	310	12.8	1.63	6.9/4.3
	G11	1400	0.5	0.35	Beech	310	10.9	1.76	6.9/3.7
Fuel	G12[a]	1400	0.5	0.3	Beech	310	12.8	1.63	6.9/4.3
	G13	1400	0.5	0.3	Pine	310	12.8	1.82	7.1/4.4
	G14	1400	0.5	0.3	Holm-oak	310	12.8	1.70	7.5/4.4
	G15	1400	0.5	0.3	Eucalyptus	310	12.8	1.59	7.9/4.5
Mean particle	G16	1400	0.5	0.3	Beech	200	12.8	1.67	6.9/4.3

Author's Post-print version. Article published in Energy & Fuels (ACS Publications):
DOI: 10.1021/ef5010557
Published version: https://pubs.acs.org/doi/abs/10.1021/ef5010557

size ($\bar{d}_p$)	G17	1400	0.5	0.3	Pine	200	12.8	1.98	7.1/4.4
	G18	1400	0.5	0.3	Holm-oak	200	12.8	1.76	7.5/4.4
	G19	1400	0.5	0.3	Eucalyptus	200	12.8	1.64	7.9/4.5
	G20	1400	0.5	0.3	Beech	500	12.8	1.58	6.9/4.3
	G21	1400	0.5	0.3	Pine	500	12.8	1.72	7.1/4.4
	G22	1400	0.5	0.3	Holm-oak	500	12.8	1.65	7.5/4.4
	G23	1400	0.5	0.3	Eucalyptus	500	12.8	1.56	7.9/4.5
	G24	1400	0.5	0.3	Beech	750	12.8	1.56	6.9/4.3
	G25	1400	0.5	0.3	Pine	750	12.8	1.68	7.1/4.4
	G26	1400	0.5	0.3	Holm-oak	750	12.8	1.61	7.5/4.4
	G27	1400	0.5	0.3	Eucalyptus	750	12.8	1.54	7.9/4.5

1 [a]Cases G7, G10, and G12 are the same as case G5.

Author's Post-print version. Article published in Energy & Fuels (ACS Publications):
DOI: 10.1021/ef5010557
Published version: https://pubs.acs.org/doi/abs/10.1021/ef5010557

1 **Figures**

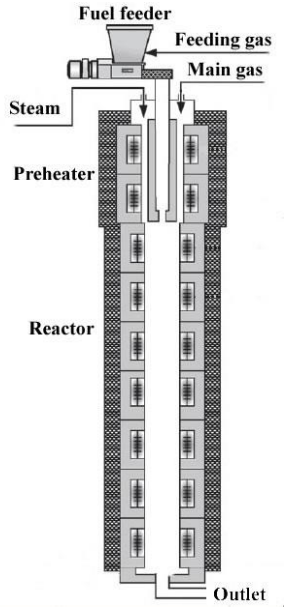

2

3 **Figure 1.** A schematic of experimental setup.[7]

Author's Post-print version. Article published in Energy & Fuels (ACS Publications):
DOI: 10.1021/ef5010557
Published version: https://pubs.acs.org/doi/abs/10.1021/ef5010557

1

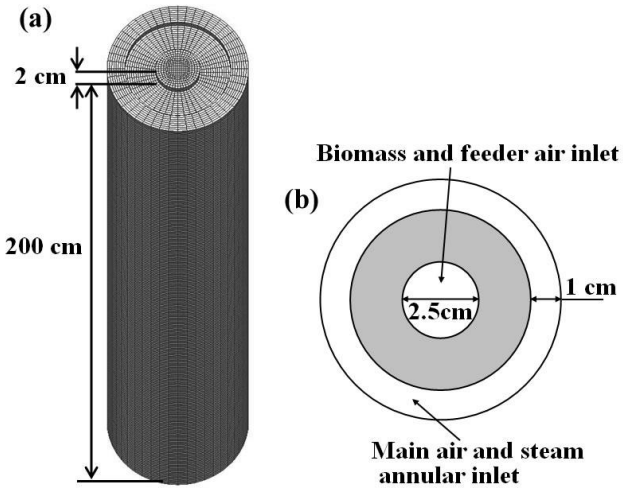

2

3

4 **Figure 2.** (a) 3D computational mesh for the DTU lab-scale entrained flow reactor and (b) the top view of

5 the reactor inlet.

6

Author's Post-print version. Article published in Energy & Fuels (ACS Publications):
DOI: 10.1021/ef5010557
Published version: https://pubs.acs.org/doi/abs/10.1021/ef5010557

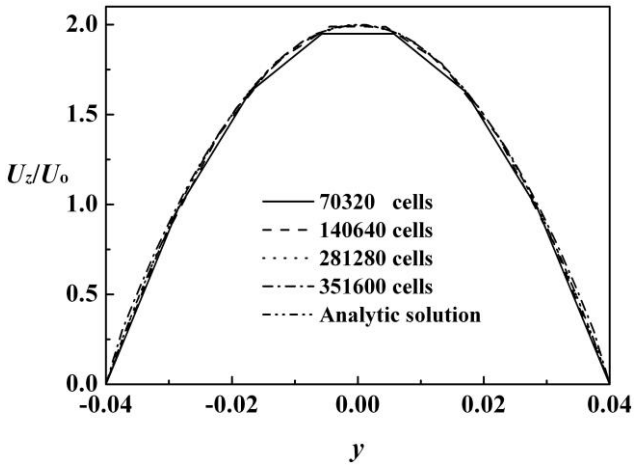

Figure 3. Velocity distribution (U_z) in the mid plane and at the bottom exit of the reactor when only air with the uniform inlet velocity U_0 is sent into the reactor.

Author's Post-print version. Article published in Energy & Fuels (ACS Publications):
DOI: 10.1021/ef5010557
Published version: https://pubs.acs.org/doi/abs/10.1021/ef5010557

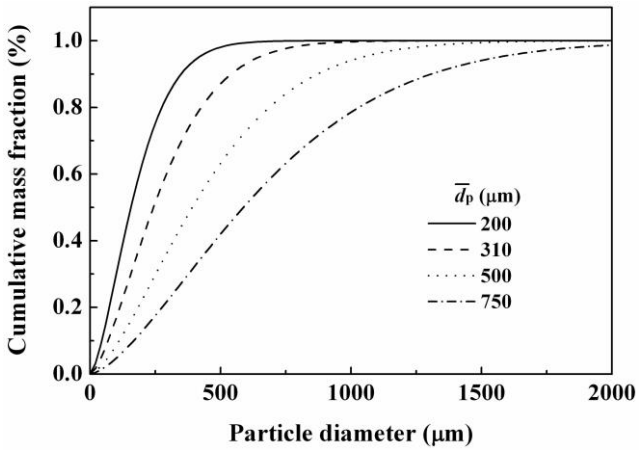

Figure 4. Biomass particle size distributions.

Author's Post-print version. Article published in Energy & Fuels (ACS Publications):
DOI: 10.1021/ef5010557
Published version: https://pubs.acs.org/doi/abs/10.1021/ef5010557

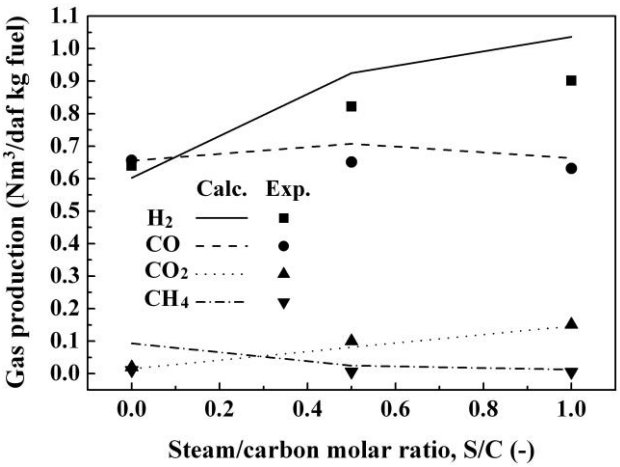

Figure 5. Species production in the product gas as a function of steam/carbon molar ratio (S/C) for pyrolysis cases (cases P1-P3 in Table 5).

Author's Post-print version. Article published in Energy & Fuels (ACS Publications):
DOI: 10.1021/ef5010557
Published version: https://pubs.acs.org/doi/abs/10.1021/ef5010557

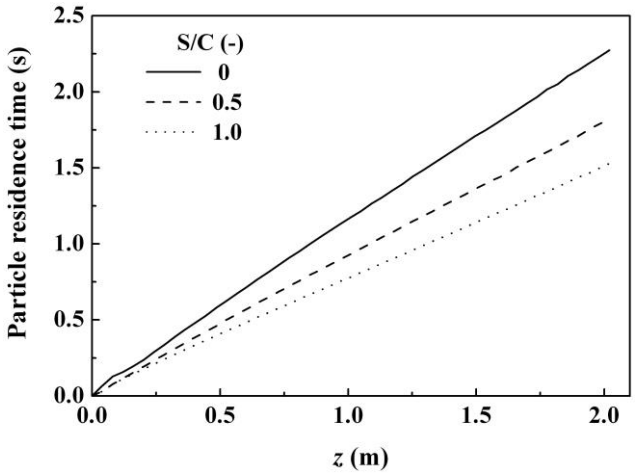

1

2 **Figure 6.** Averaged particle residence time along the reactor length at different steam/carbon molar ratio

3 (S/C) for pyrolysis cases (cases P1-P3 in Table 5).

Author's Post-print version. Article published in Energy & Fuels (ACS Publications):
DOI: 10.1021/ef5010557
Published version: https://pubs.acs.org/doi/abs/10.1021/ef5010557

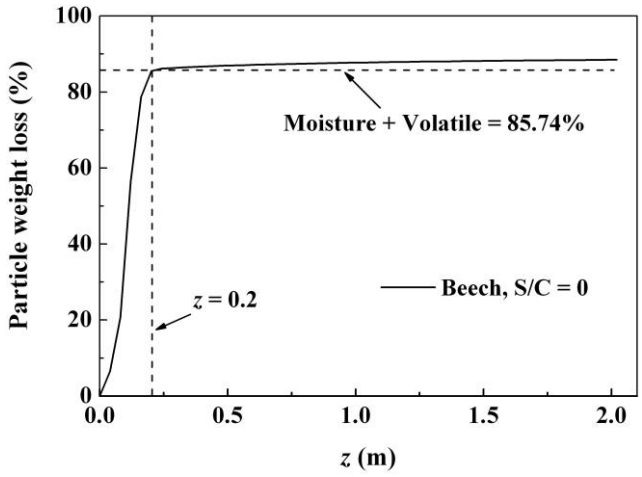

Figure 7. Averaged particle weight loss along the reactor length for the pyrolysis case (case P1 in Table 5).

Author's Post-print version. Article published in Energy & Fuels (ACS Publications):
DOI: 10.1021/ef5010557
Published version: https://pubs.acs.org/doi/abs/10.1021/ef5010557

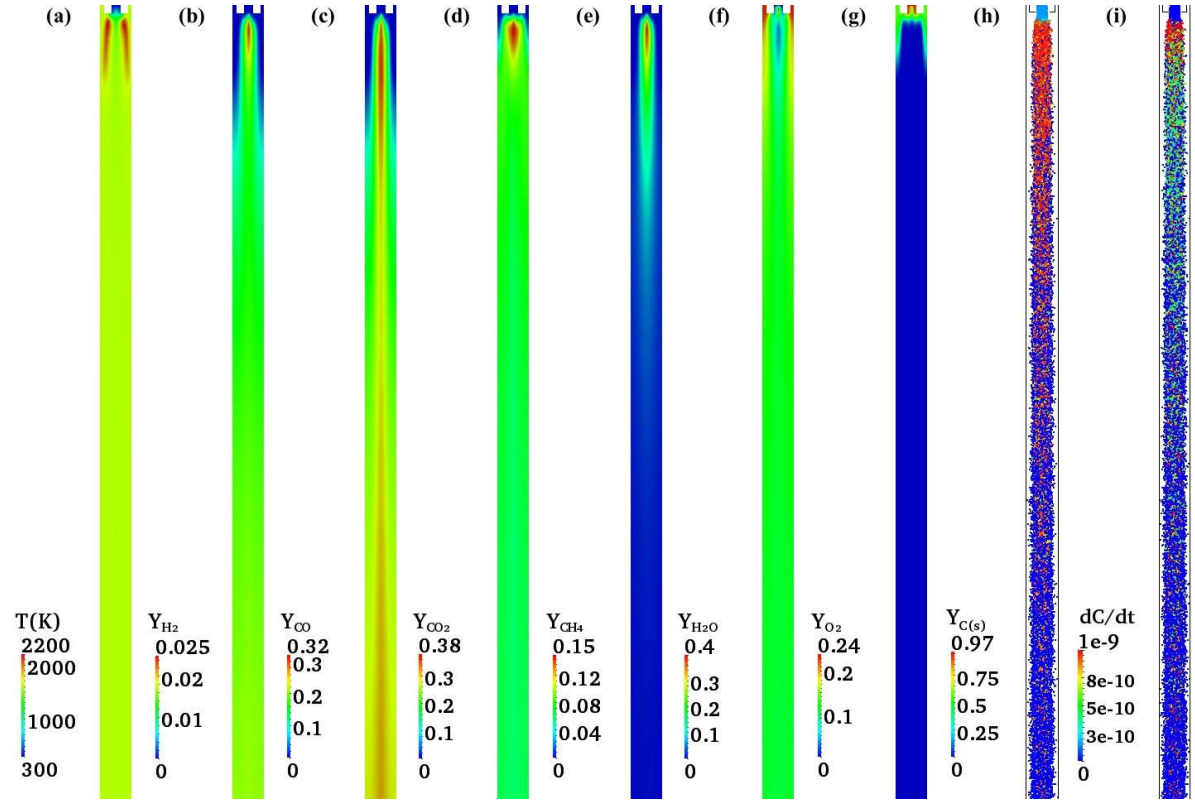

Figure 8. (a) Temperature distribution, (b-g) predictions of species mass fraction distribution in a plane passing through the axis of the reactor at *t*=10s, (h) Beech wood particle distribution colored with concentration of mass fraction of char, and (i) char burn out rate (kg/s) (case G5 in Table 5).

Author's Post-print version. Article published in Energy & Fuels (ACS Publications):
DOI: 10.1021/ef5010557
Published version: https://pubs.acs.org/doi/abs/10.1021/ef5010557

1

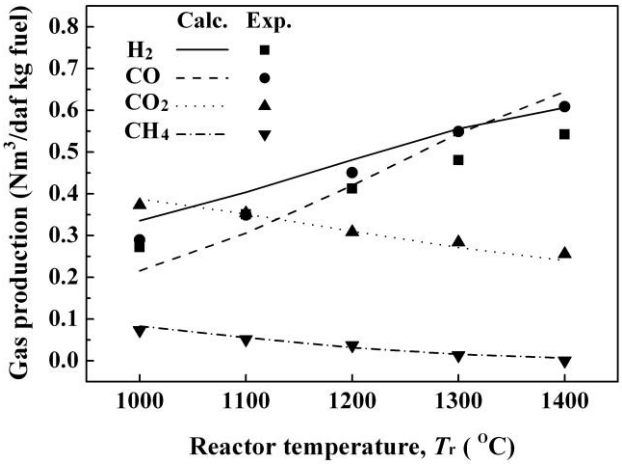

2

3 **Figure 9.** Species production as a function of reactor temperature T_r (cases G1-G5 in Table 5).

4

Author's Post-print version. Article published in Energy & Fuels (ACS Publications):
DOI: 10.1021/ef5010557
Published version: https://pubs.acs.org/doi/abs/10.1021/ef5010557

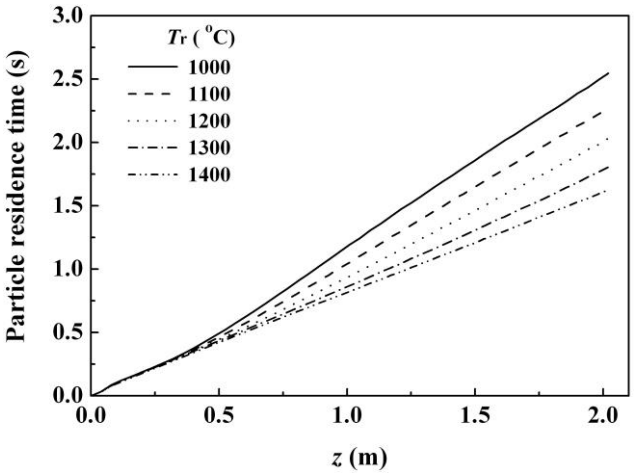

Figure 10. Averaged particle residence time along the reactor length at different reactor temperatures T_r (cases G1-G5 in Table 5).

Author's Post-print version. Article published in Energy & Fuels (ACS Publications):
DOI: 10.1021/ef5010557
Published version: https://pubs.acs.org/doi/abs/10.1021/ef5010557

1

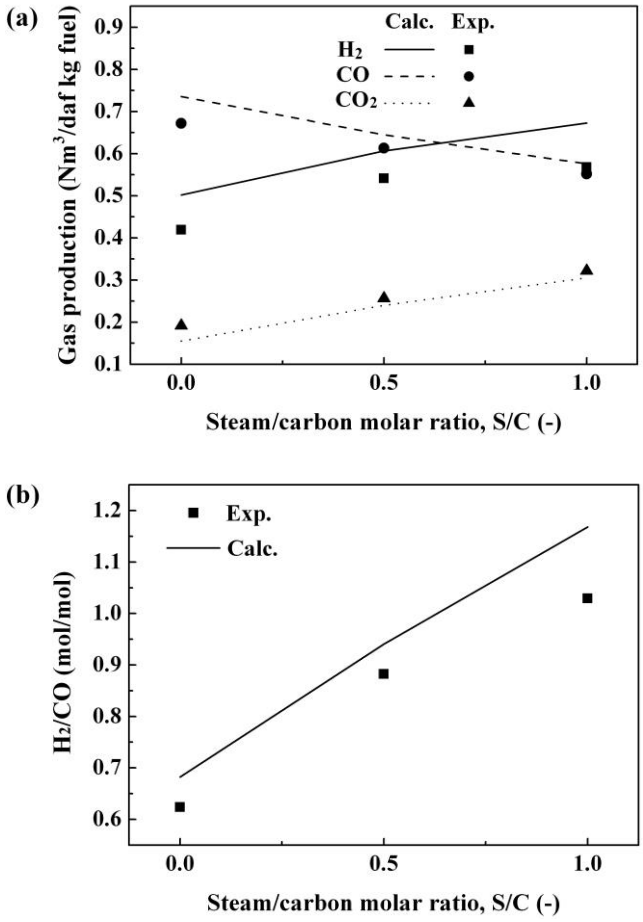

2

3

4

5 **Figure 11.** (a) Species production, and (b) H_2/CO molar ratio in the product gas as a function of

6 steam/carbon molar ratio (S/C) (cases G6-G8 in Table 5).

Author's Post-print version. Article published in Energy & Fuels (ACS Publications):
DOI: 10.1021/ef5010557
Published version: https://pubs.acs.org/doi/abs/10.1021/ef5010557

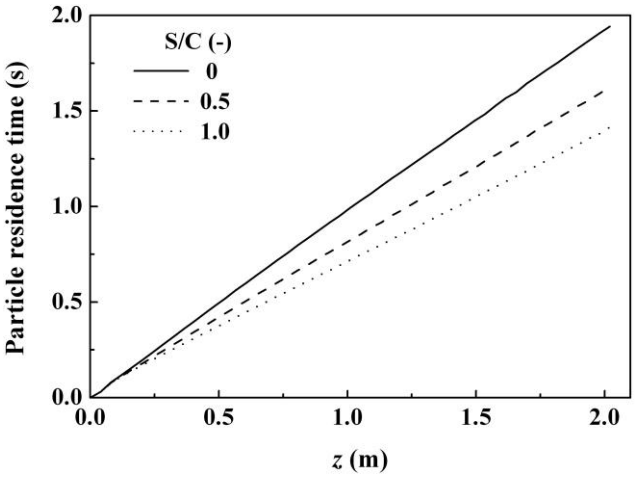

Figure 12. Averaged particle residence time along the reactor length for different steam/carbon molar ratio (S/C) (cases G6-G8 in Table 5).

Author's Post-print version. Article published in Energy & Fuels (ACS Publications):
DOI: 10.1021/ef5010557
Published version: https://pubs.acs.org/doi/abs/10.1021/ef5010557

1

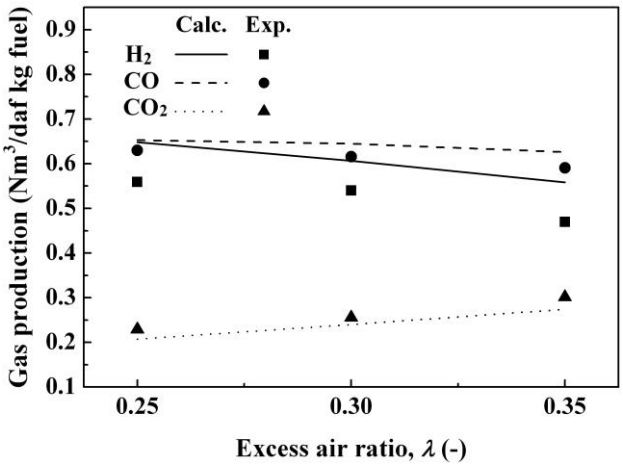

2

3 **Figure 13.** Species production as a function of excess air ratio λ (cases G9-G11 in Table 5).

4

Author's Post-print version. Article published in Energy & Fuels (ACS Publications):
DOI: 10.1021/ef5010557
Published version: https://pubs.acs.org/doi/abs/10.1021/ef5010557

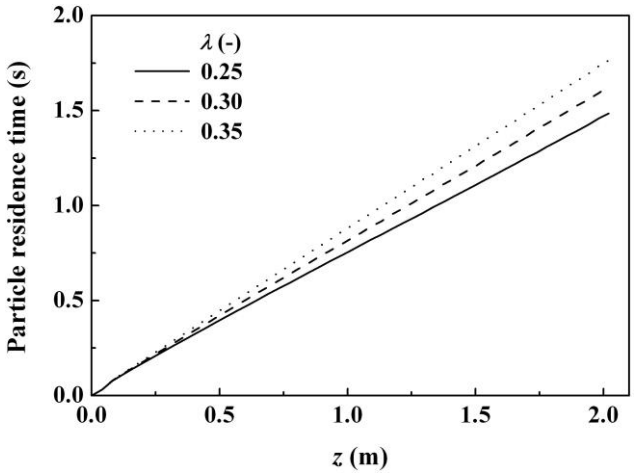

Figure 14. Averaged particle residence time along the reactor length for different excess air ratio λ (cases G9-G11 in Table 5).

Author's Post-print version. Article published in Energy & Fuels (ACS Publications):
DOI: 10.1021/ef5010557
Published version: https://pubs.acs.org/doi/abs/10.1021/ef5010557

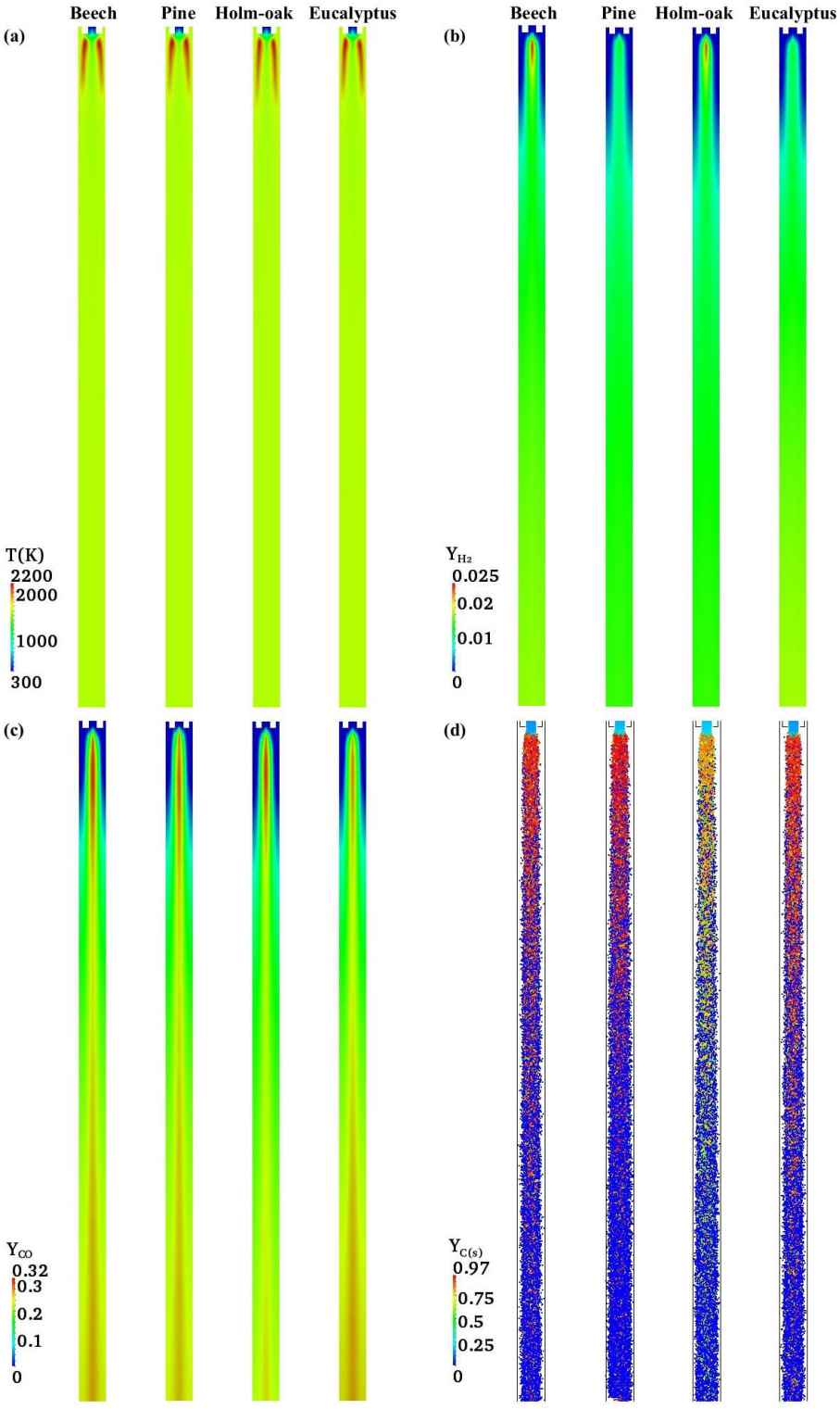

1

2 **Figure 15.** (a) Temperature distributions, mass fraction distributions of (b) H_2, (c) CO in a plane passing

3 through the axis of the reactor, and (d) fuel particle distributions colored with concentration of mass fraction

4 of char at *t*=10s for four biomasses (cases G12-G15 in Table 5).

Author's Post-print version. Article published in Energy & Fuels (ACS Publications):
DOI: 10.1021/ef5010557
Published version: https://pubs.acs.org/doi/abs/10.1021/ef5010557

1

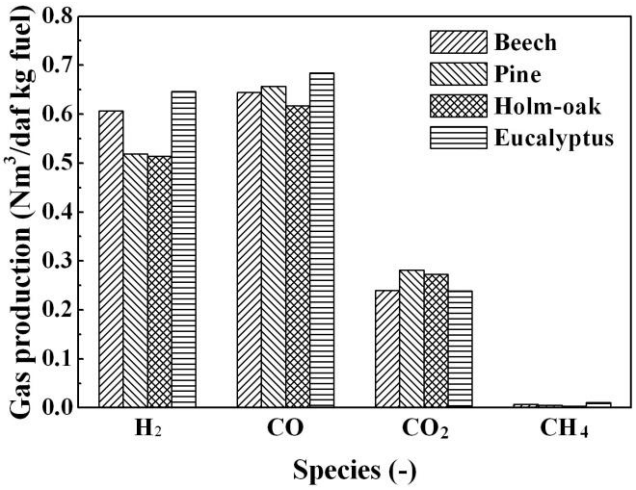

2

3 **Figure 16.** Species production at the reactor exit for different biomasses (cases G12-G15 in Table 5).

Author's Post-print version. Article published in Energy & Fuels (ACS Publications):
DOI: 10.1021/ef5010557
Published version: https://pubs.acs.org/doi/abs/10.1021/ef5010557

1

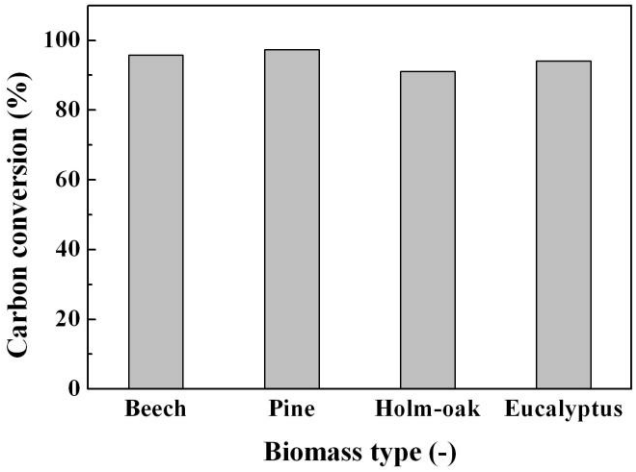

2

3 **Figure 17.** Carbon conversion at the reactor exit for different biomasses (cases G12-G15 in Table 5).

4

5

Author's Post-print version. Article published in Energy & Fuels (ACS Publications):
DOI: 10.1021/ef5010557
Published version: https://pubs.acs.org/doi/abs/10.1021/ef5010557

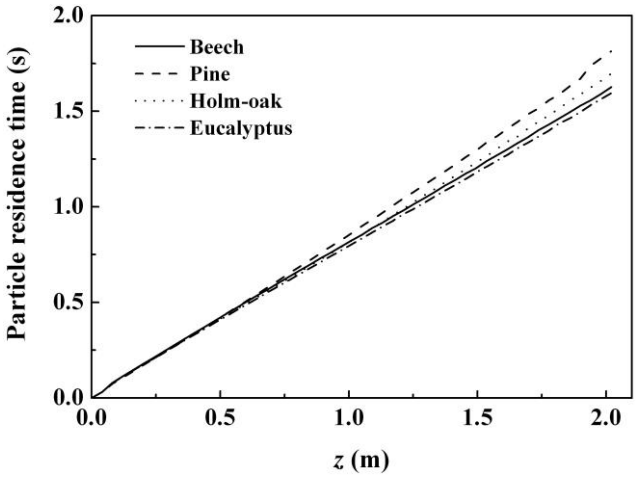

Figure 18. Averaged particle residence time along the reactor length for different biomasses (cases G12-G15 in Table 5).

Author's Post-print version. Article published in Energy & Fuels (ACS Publications):
DOI: 10.1021/ef5010557
Published version: https://pubs.acs.org/doi/abs/10.1021/ef5010557

1

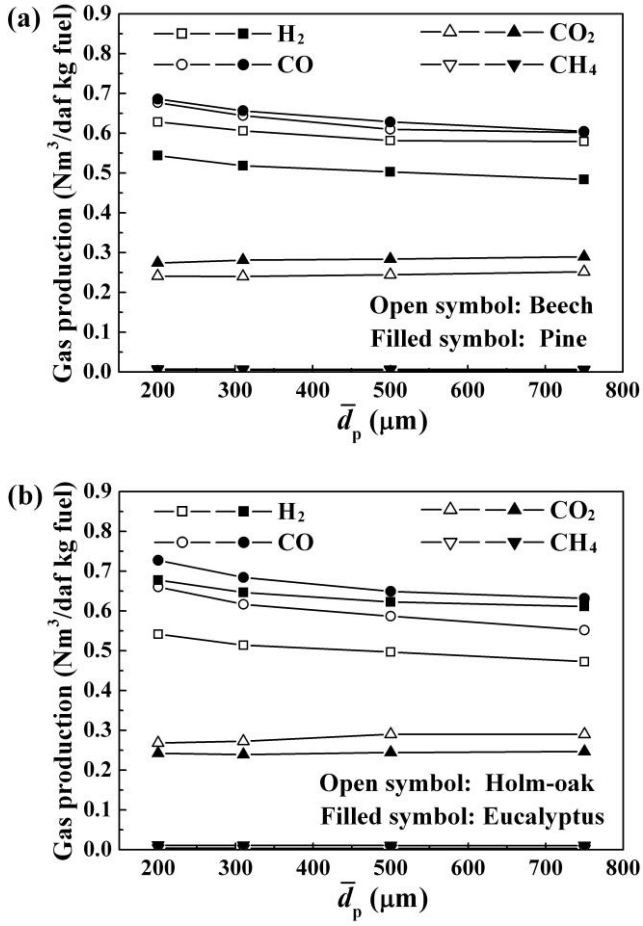

2

3

4 **Figure 19.** Species production as a function of mean particle diameter $\bar{d}_p$ (cases G12-G27 in Table 5). (a)

5 Beech and Pine, (b) Holm-oak and Eucalyptus.

Author's Post-print version. Article published in Energy & Fuels (ACS Publications):
DOI: 10.1021/ef5010557
Published version: https://pubs.acs.org/doi/abs/10.1021/ef5010557

1

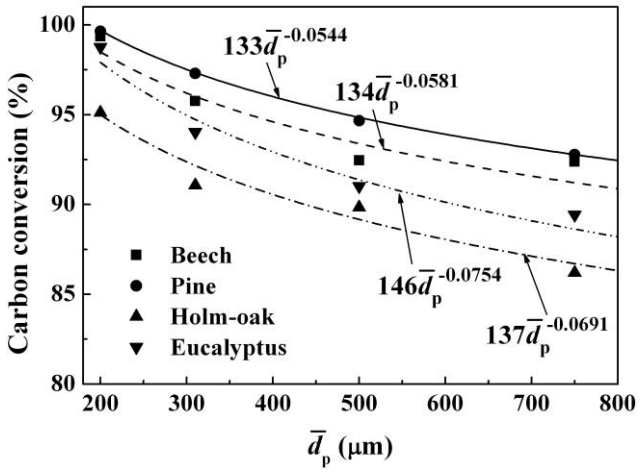

2

3 **Figure 20.** Carbon conversion as a function of mean particle diameter $\bar{d}_p$ (cases G12-G27 in Table 5).

Author's Post-print version. Article published in Energy & Fuels (ACS Publications):
DOI: 10.1021/ef5010557
Published version: https://pubs.acs.org/doi/abs/10.1021/ef5010557

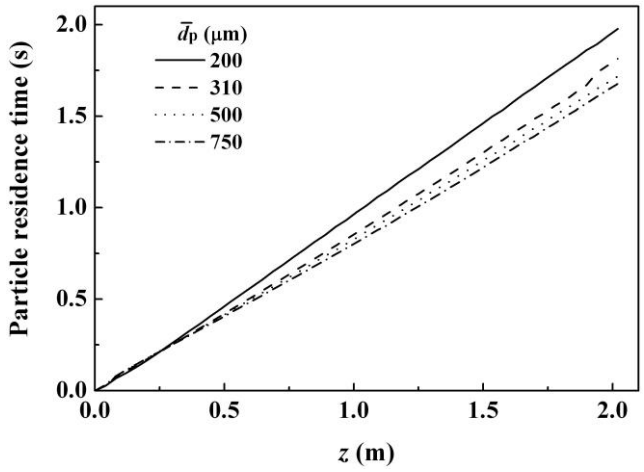

Figure 21. Averaged particle residence time along the reactor length at different mean particle diameter $\bar{d}_p$ for pine (cases G13, G17, G21, and G25 in Table 5).